

# Multi-dimensional Numerical Scheme for Resistive Relativistic MHD

Serguei S. Komissarov <sup>\*</sup>

*Department of Applied Mathematics, The University of Leeds, Leeds, LS2 9GT*

Received/Accepted

## ABSTRACT

The paper describes a new upwind conservative numerical scheme for special relativistic resistive magnetohydrodynamics with scalar resistivity. The magnetic field is kept approximately divergence free and the divergence of the electric field consistent with the electric charge distribution via the method of Generalized Lagrange Multiplier. The hyperbolic fluxes are computed using the HLL prescription and the source terms are accounted via the time-splitting technique. The results of test simulations show that the scheme can handle equally well both resistive current sheets and shock waves and thus can be a useful tool for studying phenomena of relativistic astrophysics that involve both colliding supersonic flows and magnetic reconnection.

**Key words:** methods: numerical – MHD – relativity – magnetic fields – waves

## 1 INTRODUCTION

In many phenomena of relativistic astrophysics, such as AGN, GRBs, quasars, radio galaxies, micro-quasars, pulsars and magnetars, compact X-ray binaries etc., the magnetic field is a key dynamic component. On one hand, the magnetic field drives, accelerates and partially collimates relativistic outflows from astrophysical black holes, neutron stars, and their accretion disks. On the other hand, magnetic reconnection and dissipation is responsible for bright thermal and non-thermal emission from these flows. Recent years have seen a remarkable progress in numerical methods for ideal relativistic magnetohydrodynamics (Komissarov 1999; Koide et al. 1999; Komissarov 2001; Koldoba et al. 2002; Gammie et al. 2003; Duez et al. 2005; Koide et al. 1999; Anninos et al. 2006; Shibata & Sekuguchi 2005; Anderson et al. 2006; Del Zanna et al. 2003; Antón et al. 2006; Neilsen et al. 2006; Mizuno et al. 2007; Mignone & Bode 2006; McKinney 2006; Noble et al. 2006; Giacomazzo & Rezzolla 2007; Del Zanna et al. 2007) and many interesting and important simulations have been carried out already. Quite often the numerical solutions exhibited violent magnetic reconnection. Although it is indeed very likely to occur in the considered astrophysical phenomena as the result of non-vanishing physical resistivity of plasma, both collisional and collisionless, the reconnection observed in the simulations is of purely numerical origin. It is driven by artificial resistivity arising due to truncation errors and hence fully depending on fine details of numerical schemes and resolution. A code for resistive RMHD would

allow to control magnetic reconnection according to the incorporated physical models of resistivity. Moreover, the relativistic magnetic reconnection by itself is a sufficiently rich and important physical process to warrant the effort of developing such a code. The only numerical study of relativistic magnetic reconnection so far was carried out by Watanabe & Yokoyama (2006). However, their paper gives no details of their numerical scheme and test simulations and therefore it is not clear as to how accurate their results are and how robust their numerical method is.

Since many relevant astrophysical phenomena involve shock waves, including the fast magnetic reconnection of Petcheck type (Lyubarsky 2005), a useful code should handle well not only current sheets and filaments but also shock waves. It is well known that codes that do not preserve the magnetic field divergence free can become unstable and crash in the cases with large spacial gradients. Thus this issue must be addressed too. Moreover, in the relativistic limit the spacial charge density and the advective current can become significant and thus the electric charge conservation has to be enforced. In this paper we describe the results of our efforts to construct a code that satisfies these criteria. The equations of resistive RMHD are described in Section 2. The equations of the so-called augmented system of resistive RMHD, that are designed to handle to enforce the divergence free condition for magnetic field and the electric charge conservation are presented in Section 3. The relativistic Ohm law is explained in Section 4. Section 5 gives the details of numerical integration. The test simulations are described in Section 6 and our conclusions are summarized in Section 7.

<sup>\*</sup> E-Mail: serguei@maths.leeds.ac.uk

## 2 BASIC EQUATIONS

The covariant Maxwell equations are (e.g. Jackson 1979)

$$\nabla_\beta {}^*F^{\alpha\beta} = 0, \quad (1)$$

$$\nabla_\beta F^{\alpha\beta} = I^\alpha, \quad (2)$$

where  $F^{\alpha\beta}$  is the Maxwell tensor of the electromagnetic field,  ${}^*F^{\alpha\beta}$  is the Faraday tensor, and  $I^\alpha$  is the 4-vector of electric current.

In highly ionized plasma, including pair plasma, the electric and magnetic susceptibilities are essentially zero and one has

$${}^*F^{\alpha\beta} = \frac{1}{2}e^{\alpha\beta\mu\nu} F_{\mu\nu} \quad (3)$$

$$F^{\alpha\beta} = -\frac{1}{2}e^{\alpha\beta\mu\nu} {}^*F_{\mu\nu}, \quad (4)$$

where

$$e_{\alpha\beta\mu\nu} = \sqrt{-g} \epsilon_{\alpha\beta\mu\nu}, \quad (5)$$

is the Levi-Civita alternating tensor of space-time and  $\epsilon_{\alpha\beta\mu\nu}$  is the four-dimensional Levi-Civita symbol.

In the coordinate basis of global inertial frame of special relativity these equations split into the familiar set

$$\nabla \cdot \mathbf{B} = 0, \quad (6)$$

$$\partial_t \mathbf{B} + \nabla \times \mathbf{E} = 0, \quad (7)$$

$$\nabla \cdot \mathbf{E} = q, \quad (8)$$

$$-\partial_t \mathbf{E} + \nabla \times \mathbf{B} = \mathbf{J}, \quad (9)$$

where

$$E^i = F^{ti} = \frac{1}{2}e^{ijk} {}^*F_{jk}, \quad (10)$$

$$B^i = {}^*F^{it} = \frac{1}{2}e^{ijk} F_{jk}, \quad (11)$$

$$q = I^t, \quad J^k = I^k. \quad (12)$$

are the electric field, the magnetic field, the electric charge density, and the electric current density respectively as measured by the inertial observer ( $e_{ijk} = e_{0ijk}$  is the Levi-Civita tensor of space.). These equations are consistent with the electric charge conservation

$$\partial_t q + \nabla \cdot \mathbf{J} = 0. \quad (13)$$

In magnetohydrodynamics Maxwell's equations are supplemented with the equations of motion of matter and the continuity equation. In the covariant form the equations of motion can be written as

$$\nabla_\nu T^{\mu\nu} = 0 \quad (14)$$

where the total stress-energy momentum tensor,

$$T^{\mu\nu} = T_{(m)}^{\mu\nu} + T_{(e)}^{\mu\nu}, \quad (15)$$

is the sum of the stress-energy momentum tensor of the electromagnetic field

$$T_{(e)}^{\mu\nu} = F^{\mu\gamma} F_{\gamma}^{\nu} - \frac{1}{4}(F^{\alpha\beta} F_{\alpha\beta})g^{\mu\nu}, \quad (16)$$

and the stress-energy momentum tensor of matter

$$T_{(m)}^{\mu\nu} = wu^\mu u^\nu + pg^{\mu\nu}. \quad (17)$$

Here where  $p$  is the thermodynamic pressure,  $w(p, \rho)$  is the relativistic enthalpy per unit volume as measured in the rest frame of fluid ( $w$  includes the rest mass-energy density of matter  $\rho$ ), and  $u^\nu$  is the fluid 4-velocity. In the global inertial frame with time-independent coordinate grid eq.14 splits into the energy and momentum conservation laws

$$\partial_t e + \nabla \cdot \mathbf{S} = 0, \quad (18)$$

$$\partial_t \mathbf{P} + \nabla \cdot \mathbf{\Pi} = 0, \quad (19)$$

where

$$e = \frac{1}{2}(E^2 + B^2) + w\gamma^2 - p \quad (20)$$

is the energy density,

$$\mathbf{S} = \mathbf{E} \times \mathbf{B} + w\gamma^2 \mathbf{v}, \quad (21)$$

is the energy flux density,

$$\mathbf{P} = \mathbf{E} \times \mathbf{B} + w\gamma^2 \mathbf{v} \quad (22)$$

is the momentum density, and

$$\mathbf{\Pi} = -\mathbf{E}\mathbf{E} - \mathbf{B}\mathbf{B} + w\gamma^2 \mathbf{v}\mathbf{v} + \left(\frac{1}{2}(E^2 + B^2) + p\right) \mathbf{g} \quad (23)$$

is the stress tensor. Here  $\gamma$  is the Lorentz factor,  $\mathbf{v}$  is the velocity as measured by the inertial observer, and  $\mathbf{g}$  is the metric tensor of space.

The covariant continuity equation is

$$\nabla_\nu \rho u^\nu = 0, \quad (24)$$

where  $\rho$  is the rest mass density as measured in the rest frame of fluid. In the inertial frame this reads

$$\partial_t \rho \gamma + \nabla \cdot (\rho \gamma \mathbf{v}) = 0. \quad (25)$$

Equations (6,7,8,9,13,18,19,25) constitute the 3+1 PDE system of relativistic magnetohydrodynamics in special relativity. Once supplemented with equations of state, that relate various thermodynamic parameters of matter, and with the Ohm law, that couples matter and the electromagnetic field, this system closes.

## 3 AUGMENTED SYSTEM

As well known, the divergence free condition (6) for the magnetic field can be treated as a constraint on the initial solution of Cauchy problem because the Faraday equation (7) will then ensure that the magnetic field remains divergence free at any time. The equation of electric charge conservation is also not independent and follows from the Ampere equation (9) and the Gauss law (8). These properties of the differential equations are not preserved by many numerical schemes. Indeed, the most straightforward way of constructing a self-consistent finite difference counterpart for a differential system like electrodynamics is to ignore all constraints (non-evolution equations) and to leave out all the supplementary laws like the electric charge conservation (otherwise the system of finite difference equations becomes over-determined). However, it has been discovered that this lack of consistency may lead to strong corruption of numerical solutions in regions with large truncation errors, like strong discontinuities, and even cause code crash. In ideal

MHD the divergence free condition has been found particularly important. A number of techniques has been proposed to combat the problem. Here we adopt the so-called Generalized Lagrange Multiplier method developed by Munz et al.(1999). The main idea is to create a new, augmented system of differential equations, that will include only evolution equations and will have the same solutions of the Cauchy problem as the original system provided the initial solution satisfies the differential constraints of the original system. If, however, the initial solution does not satisfy the constraints then the deviations should decay or at least move away as relatively high speed waves. This will ensure that the deviations caused by truncation errors of a numerical method for the augmented system remain small.

To deal with the divergence free constraint we modify eqs.(6,7) so that they become

$$\partial_t \Phi + \nabla \cdot \mathbf{B} = -\kappa \Phi, \quad (26)$$

$$\partial_t \mathbf{B} + \nabla \times \mathbf{E} + \nabla \Phi = 0, \quad (27)$$

where  $\Phi$  is a new dynamic variable (pseudo-potential). From these equations it follows that  $\Phi$  satisfies the telegraph equation

$$-\partial_t^2 \Phi - \kappa \partial_t \Phi + \nabla^2 \Phi = 0. \quad (28)$$

Thus,  $\Phi$  is transported by hyperbolic waves propagating with the speed of light and decays if  $\kappa > 0$ . For positive  $\kappa$  the natural evolution of  $\Phi$  is toward  $\Phi(\mathbf{r}, t) = 0$  (unless prevented by boundary conditions) and eq.(26) shows that this final state implies divergence free magnetic field. In fact, it is easy to see that the divergence of magnetic field also satisfies the same telegraph equation

$$-\partial_t^2 (\nabla \cdot \mathbf{B}) - \kappa \partial_t (\nabla \cdot \mathbf{B}) + \nabla^2 (\nabla \cdot \mathbf{B}) = 0, \quad (29)$$

and thus evolves in the same fashion.

To deal with the Gauss law we modify eqs.(8,9) so they read

$$\partial_t \Psi + \nabla \cdot \mathbf{E} = q - \kappa \Psi, \quad (30)$$

$$-\partial_t \mathbf{E} + \nabla \times \mathbf{B} - \nabla \Psi = \mathbf{J}, \quad (31)$$

where  $\Psi$  is another new dynamic variable. From these two equations and the electric charge conservation it follows that the evolution of  $\Psi$  is again described by the telegraph equation

$$-\partial_t^2 \Psi - \kappa \partial_t \Psi + \nabla^2 \Psi = 0. \quad (32)$$

(Although in principle one could use different constants  $\kappa$  for  $\Phi$  and  $\Psi$  this brings no benefit.) Thus,  $\Psi$ , naturally evolves in the same fashion as  $\Phi$ , ensuring that the electrodynamic solution is kept consistent with the Gauss law. Similarly, one finds that

$$-\partial_t^2 (\nabla \cdot \mathbf{E} - q) - \kappa \partial_t (\nabla \cdot \mathbf{E} - q) + \nabla^2 (\nabla \cdot \mathbf{E} - q) = 0. \quad (33)$$

Summarizing, the augmented system of relativistic MHD is

$$\partial_t \Phi + \nabla \cdot \mathbf{B} = -\kappa \Phi, \quad (34)$$

$$\partial_t \mathbf{B} + \nabla \times \mathbf{E} + \nabla \Phi = 0, \quad (35)$$

$$\partial_t \Psi + \nabla \cdot \mathbf{E} = q - \kappa \Psi, \quad (36)$$

$$-\partial_t \mathbf{E} + \nabla \times \mathbf{B} - \nabla \Psi = \mathbf{J}, \quad (37)$$

$$\partial_t q + \nabla \cdot \mathbf{J} = 0. \quad (38)$$

$$\partial_t \rho \gamma + \nabla \cdot \rho \gamma \mathbf{v} = 0, \quad (39)$$

$$\partial_t e + \nabla \cdot \mathbf{S} = 0, \quad (40)$$

$$\partial_t \mathbf{P} + \nabla \cdot \mathbf{\Pi} = 0, \quad (41)$$

where

$$e = \frac{1}{2}(E^2 + B^2) + w\gamma^2 - p \quad (42)$$

$$\mathbf{S} = \mathbf{E} \times \mathbf{B} + w\gamma^2 \mathbf{v}, \quad (43)$$

$$\mathbf{P} = \mathbf{E} \times \mathbf{B} + w\gamma^2 \mathbf{v} \quad (44)$$

$$\mathbf{\Pi} = -\mathbf{E}\mathbf{E} - \mathbf{B}\mathbf{B} + w\gamma^2 \mathbf{v}\mathbf{v} + \left(\frac{1}{2}(E^2 + B^2) + p\right) \mathbf{g} \quad (45)$$

Every differential equation of the system is an evolution equation and a conservation law (with or without a source term), and there is wealth of numerical methods for such systems. For example one could use Godunov's upwind scheme (Godunov 1959) or one of its numerous higher order "children". This simplicity of numerical implementation is the main advantage of the method of Generalized Lagrange Multiplier.

#### 4 OHM'S LAW

In this paper we consider only the simplest case of scalar resistivity. In strong magnetic field the resistivity (conductivity) becomes anisotropic and the tensor description becomes more appropriate. We will consider this case in future.

The covariant form of scalar Ohm's law is

$$I_\nu = \sigma F_{\nu\mu} u^\mu + q_0 u_\nu, \quad (46)$$

where  $\sigma = 1/\eta$  is the conductivity,  $\eta$  is the resistivity, and  $q_0 = -I_\nu u^\nu$  is the electric charge density as measured in the fluid frame (Blackman & Field 1993; Lyutikov & Uzdensky 2003). In the general inertial frame this reads

$$\mathbf{J} = \sigma \gamma [\mathbf{E} + \mathbf{v} \times \mathbf{B} - (\mathbf{E} \cdot \mathbf{v}) \mathbf{v}] + q \mathbf{v}, \quad (47)$$

whereas in the fluid frame one has the usual Ohm law

$$\mathbf{J} = \sigma \mathbf{E}. \quad (48)$$

In the limit of infinite conductivity ( $\sigma \rightarrow \infty$ ) eq.(47) reduces to

$$\mathbf{E} + \mathbf{v} \times \mathbf{B} - (\mathbf{E} \cdot \mathbf{v}) \mathbf{v} = 0.$$

Splitting this equation into the components that are normal and parallel to the velocity vector one obtains

$$\mathbf{E}_\perp + \mathbf{v} \times \mathbf{B} = 0$$

and

$$\mathbf{E}_\parallel - (\mathbf{E} \cdot \mathbf{v}) \mathbf{v} = 0.$$

These show that  $E_\parallel = 0$  and thus one has the usual result

$$\mathbf{E} = -\mathbf{v} \times \mathbf{B}, \quad (49)$$

the purely inductive electric field.

Now consider the reduced form of Ampere's law

$$-\partial_t \mathbf{E} = \mathbf{J}, \quad (50)$$

which is of interest for numerical schemes using time-splitting technique. When splitted into components normal and parallel to the velocity vector this equation reads

$$\partial_t \mathbf{E}_{\parallel} + \sigma\gamma[\mathbf{E}_{\parallel} - (\mathbf{E} \cdot \mathbf{v})\mathbf{v}] = 0, \quad (51)$$

$$\partial_t \mathbf{E}_{\perp} + \sigma\gamma[\mathbf{E}_{\perp} + \mathbf{v} \times \mathbf{B}] = 0. \quad (52)$$

The solutions of initial value problem for these linear equations are

$$\mathbf{E}_{\parallel} = \mathbf{E}_{\parallel}^0 \exp\left(-\frac{\sigma}{\gamma}t\right), \quad (53)$$

and

$$\mathbf{E}_{\perp} = \mathbf{E}_{\perp}^* + (\mathbf{E}_{\perp}^0 - \mathbf{E}_{\perp}^*) \exp(-\sigma\gamma t), \quad (54)$$

where  $\mathbf{E}_{\perp}^* = -\mathbf{v} \times \mathbf{B}$  and suffix 0 denotes the initial values. One can see that for relativistic flows the normal component of electric field approaches the inductive value  $\mathbf{E}_{\perp}^*$  faster than the parallel component approaches zero.

## 5 NUMERICAL METHOD

The evolution equations (34-41) can be written as conservation laws. In Cartesian coordinates, and this is the only type of coordinates we use in the paper, the system can be written as a single phase vector equation

$$\frac{\partial \mathcal{Q}(\mathcal{P})}{\partial t} + \frac{\partial \mathcal{F}^m(\mathcal{P})}{\partial x^m} = \mathcal{S}(\mathcal{P}), \quad (55)$$

where

$$\mathcal{Q} = \begin{pmatrix} \Phi \\ B^i \\ \Psi \\ E^i \\ q \\ \rho\gamma \\ e \\ P^i \end{pmatrix}, \quad \mathcal{P} = \begin{pmatrix} \Phi \\ B^i \\ \Psi \\ E^i \\ q \\ \rho \\ p \\ u^i \end{pmatrix}, \quad \mathcal{S} = \begin{pmatrix} -\kappa\Psi \\ 0^i \\ q - \kappa\Psi \\ -J^i \\ 0 \\ 0 \\ 0 \\ 0^i \end{pmatrix}$$

are the vectors of conserved quantities, primitive quantities, and sources respectively and

$$\mathcal{F}^m = \begin{pmatrix} B^m \\ e^{imk} E_k + \Phi g^{im} \\ E^j \\ -e^{imk} B_k + \Psi g^{im} \\ J^m \\ \rho u^m \\ S^m \\ \Pi^{im} \end{pmatrix}$$

is the vector of corresponding hyperbolic fluxes. Here  $u^i = \gamma v^i$  are the spatial components of 4-velocity,  $g^{ij}$  are the components of the metric tensor of space (given by Kronecker's delta  $\delta^{ij}$ ),  $e^{ijk}$  is the Levi-Civita alternating tensor of space.

We have found useful to split the source term into two parts

$$\mathcal{S}_a(\mathcal{P}) = \begin{pmatrix} 0 \\ 0^i \\ q \\ -qv^i \\ 0 \\ 0 \\ 0 \\ 0^i \end{pmatrix} \quad \text{and} \quad \mathcal{S}_b(\mathcal{P}) = \begin{pmatrix} -\kappa\Phi \\ 0^i \\ -\kappa\Psi \\ -J_c^i \\ 0 \\ 0 \\ 0 \\ 0^i \end{pmatrix},$$

where

$$\mathbf{J}_c = \sigma\gamma[\mathbf{E} + \mathbf{v} \times \mathbf{B} - (\mathbf{E} \cdot \mathbf{v})\mathbf{v}]$$

is the conductivity current. The source term  $\mathcal{S}_b$  is potentially stiff (in the case of low resistivity) and is treated via the time-step splitting technique by Strang (1968). That is first the solution is advanced via integration of equation

$$\frac{\partial \mathcal{Q}(\mathcal{P})}{\partial t} = \mathcal{S}_b(\mathcal{P}), \quad (56)$$

over the half time-step,  $\Delta t/2$ . Then the solution is advanced via second-order accurate numerical integration of equation

$$\frac{\partial \mathcal{Q}(\mathcal{P})}{\partial t} + \frac{\partial \mathcal{F}^m(\mathcal{P})}{\partial x^m} = \mathcal{S}_a(\mathcal{P}), \quad (57)$$

over the full time-step. Finally, the solution is advanced via integration of equation (56) over the half time-step once more. Thanks to the fact that all equations in (56) are linear the integration is carried out using analytic solutions, in particular solutions (53,54) are utilized at this stage. This removes stability constraints of the time step otherwise imposed by  $\mathcal{S}_b$ . In principle all source terms could be passed to eq.(56) but this somehow results in reduction of accuracy.

Equation (57) is integrated explicitly

$$\mathcal{Q}_{n+1} = \mathcal{Q}_n + \Delta t \sum_{m=1}^{N_d} \frac{\mathcal{F}_{m-\frac{1}{2},n+\frac{1}{2}} - \mathcal{F}_{m+\frac{1}{2},n+\frac{1}{2}}}{\Delta x^m} + \Delta t \mathcal{S}_{a,n+\frac{1}{2}}. \quad (58)$$

Here  $\mathcal{Q}_n$  is the conserved quantity of a cell at  $t = t_n$ ,  $\mathcal{Q}_{n+1}$  is the conserved quantity of this cell at  $t = t_n + \Delta t$ ,  $\mathcal{S}_{a,n+\frac{1}{2}}$  is the source term of the cell at  $t = t_n + \Delta t/2$ ,  $\mathcal{F}_{m+\frac{1}{2},n+\frac{1}{2}}$  is the flux through the right interface and  $\mathcal{F}_{m-\frac{1}{2},n+\frac{1}{2}}$  is the flux through the left interface of the cell normal to the direction of  $x^m$  at time  $t = t_n + \Delta t/2$ .  $\Delta x^m$  is the cell size in this direction and  $N_d$  is the number of spatial dimensions.

To determine the sources and fluxes at half time-step the solution is temporarily advances via

$$\mathcal{Q}_{n+\frac{1}{2}} = \mathcal{Q}_n + \frac{\Delta t}{2} \sum_{m=1}^{N_d} \frac{\mathcal{F}_{m-\frac{1}{2},n} - \mathcal{F}_{m+\frac{1}{2},n}}{\Delta x^m} + \frac{\Delta t}{2} \mathcal{S}_{a,n}. \quad (59)$$

The interface fluxes  $\mathcal{F}_{m+\frac{1}{2},n}$  are computed using the HLL-prescription (Harten et al. 1983):

$$\mathcal{F}_{m+\frac{1}{2},n} = \frac{\mathcal{F}_{m+\frac{1}{2},n}^R + \mathcal{F}_{m+\frac{1}{2},n}^L}{2} - \frac{\mathcal{Q}_{m+\frac{1}{2},n}^R - \mathcal{Q}_{m+\frac{1}{2},n}^L}{2}, \quad (60)$$

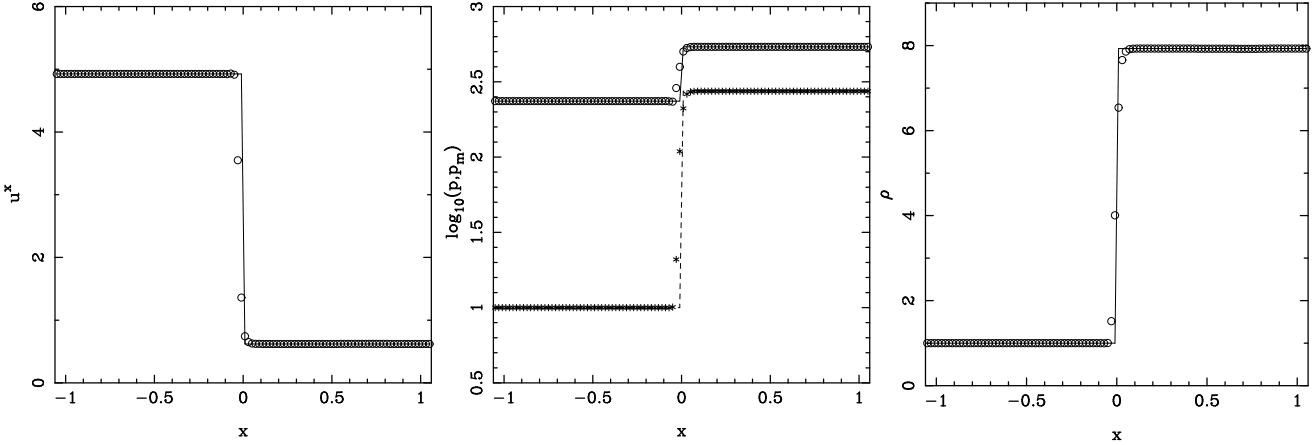


**Figure 1.** Stationary fast shock. *Left panel:*  $u^x = \gamma v^x$ ; *Middle panel:* gas pressure (dashed line and stars) and magnetic pressure (solid line and circles); *Right panel* rest mass density,  $\rho$ .

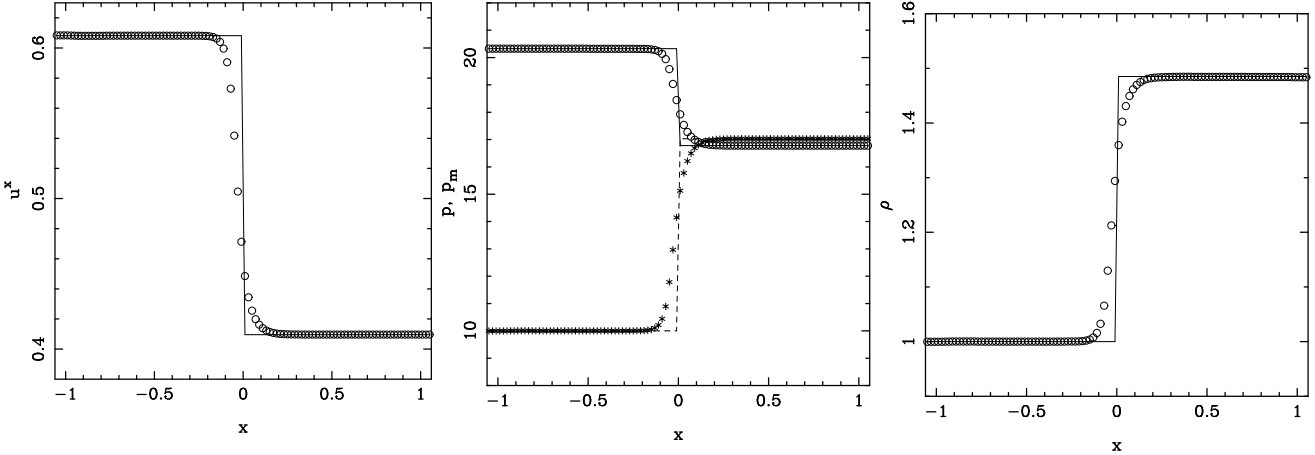


**Figure 2.** Stationary slow shock. *Left panel:*  $u^x = \gamma v^x$ ; *Middle panel:* gas pressure (dashed line and stars) and magnetic pressure (solid line and circles); *Right panel* rest mass density,  $\rho$ .

where indexes  $L$  and  $R$  refer to the states respectively to the left and to the right of the interface (which can be considered as the location of discontinuity in the solution at  $t = t_n$ ). Note the simplification of the general HLL prescription due to the fact that the maximum characteristic speed of the system in each direction equals exactly to the speed of light (unity in our dimensionless equations). For the auxiliary half time-step these left and right states are found via the piecewise constant reconstruction of numerical solution in each spatial direction

$$\mathcal{P}_n = \mathcal{P}_n^c \quad \text{for} \quad x_c^m - \frac{\Delta x^m}{2} < x^m < x_c^m + \frac{\Delta x^m}{2}, \quad (61)$$

where  $x_c^m$  is the coordinate of the cell center and  $\mathcal{P}_n$  is the phase state vector of the cell.

The auxiliary solution is then used for another, now quadratic reconstruction of numerical solution within each cell

$$\begin{aligned} \mathcal{P}_{n+\frac{1}{2}} &= \mathcal{P}_{n+\frac{1}{2}}^c + a_1(x^m - x_c^m) + \frac{a_2}{2}(x^m - x_c^m)^2 \\ \text{for} \quad x_c^m - \frac{\Delta x^m}{2} &< x^m < x_c^m + \frac{\Delta x^m}{2}. \end{aligned} \quad (62)$$

Obviously,  $a_1$  and  $a_2$  are the first and the second order derivatives of the reconstructed solution and these are to be found from the numerical solution using one of many existing non-linear limiters (needed to avoid spurious oscillations). In this particular paper  $a_1$  is found using the same limiter as in our ideal MHD code (Komissarov 1999)

$$a_1 = \text{av}(\mathcal{P}'_L, \mathcal{P}'_R) \quad (63)$$

where

$$\mathcal{P}'_L = \frac{\mathcal{P}_i - \mathcal{P}_{i-1}}{\Delta x^m}, \quad \mathcal{P}'_R = \frac{\mathcal{P}_{i+1} - \mathcal{P}_i}{\Delta x^m},$$

are the left and right numerical approximations of the first derivative ( $i$  is the cell index along the direction of  $x^m$ ), and

$$\text{av}(a, b) = \begin{cases} 0 & \text{if } ab < 0 \text{ or } a^2 + b^2 = 0, \\ \frac{a^2 b + a b^2}{a^2 + b^2} & \text{if } ab \geq 0 \text{ and } a^2 + b^2 \neq 0 \end{cases} \quad (64)$$

To find  $a_2$  we use a similar procedure. First we compute the left, center, and right numerical approximations for the second derivative,  $\mathcal{P}''_L$ ,  $\mathcal{P}''_C$ , and  $\mathcal{P}''_R$ , and then we feed them to the minmod function with three arguments

$$a_2 = \text{minmod}(\mathcal{P}''_L, \mathcal{P}''_C, \mathcal{P}''_R), \quad (65)$$

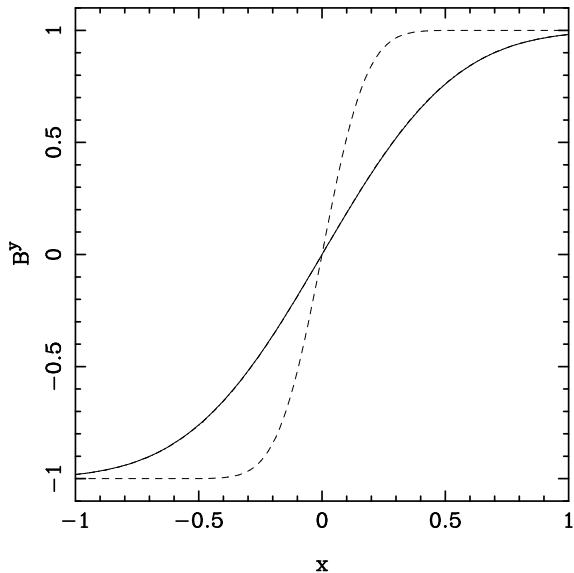


**Figure 5.** Self-similar current sheet. The dashed and the dash-dotted lines show the exact solution at  $t = 1$  and  $t = 9$  respectively. The solid line shows the numerical solution at  $t = 9$ ; it is indistinguishable from the exact solution on this plot.

where

$$\text{minmod}(a, b, c) = \begin{cases} 0 & \text{if } ab \leq 0 \text{ or } bc \leq 0 \\ \min(a, b, c) & \text{if } a, b, c > 0 \\ \max(a, b, c) & \text{if } a, b, c < 0 \end{cases} \quad (66)$$

The left and right states of each cell interface that are found via this second reconstruction are then used to compute HLL-fluxes  $\mathcal{F}_{m+\frac{1}{2}, n+\frac{1}{2}}$  of equation (58). The resulting scheme is second order accuracy in time and third order accuracy in space.

## 6 TEST SIMULATIONS

In these test simulations we use the polytropic equation of state

$$w = \rho + \frac{\Gamma}{\Gamma - 1} p \quad (67)$$

with the ratio of specific heats  $\Gamma = 4/3$ .

### 6.1 One-dimensional test problems

#### 6.1.1 Stationary Fast Shock

To set up this test we solved the ideal relativistic MHD shock equations describing stationary shocks. The selected particular solution is

*Left state:*

$$\mathbf{B} = (5.0, 15.08, 0.0), \quad \gamma \mathbf{v} = (4.925, 0.0, 0.0), \quad \rho = 1.0, \\ p = 10.0, \quad q = 0, \quad \Phi = 0, \quad \Psi = 0;$$

*Right state:*

$$\mathbf{B} = (5.0, 28.92, 0.0), \quad \gamma \mathbf{v} = (0.6209, 0.1009, 0.0), \quad \rho = 7.930, \\ p = 274.1; \quad q = 0, \quad \Phi = 0, \quad \Psi = 0.$$

The electric field is found via the ideal equation

$$-\mathbf{E} = -\mathbf{v} \times \mathbf{B}. \quad (68)$$

The computational grid is uniform and has 100 cells in  $[-1, +1]$  and the initial solution is set as a discontinuity at  $x = 0$ . The resistivity is  $\eta = 0.01$ . Figure 1 shows the numerical solution at  $t = 3.0$  by when the secondary waves created during the development of the dissipative shock structure have left the grid. One can see that the shock jump is captured very well. The fact that there are only 3 grid points in the shock structure tells that the shock is unresolved and suggests that the shock structure might be dominated by numerical dissipation. This is confirmed by the simulations with higher resistivity (see fig.3).

#### 6.1.2 Stationary Slow Shock

To set up this test we also solved the ideal relativistic MHD shock equations describing stationary shocks. Now the selected particular solution is

*Left state:*

$$\mathbf{B} = (5.0, 3.511, 0.0), \quad \gamma \mathbf{v} = (0.6082, 0.0, 0.0), \quad \rho = 1.0, \\ p = 10.0, \quad q = 0, \quad \Phi = 0, \quad \Psi = 0;$$

*Right state:*

$$\mathbf{B} = (5.0, 2.287, 0.0), \quad \gamma \mathbf{v} = (0.4096, -0.2147, 0.0), \quad \rho = 1.485, \\ p = 17.03; \quad q = 0, \quad \Phi = 0, \quad \Psi = 0.$$

The computational grid is uniform and has 100 cells in  $[-1, +1]$  and the initial solutions is a discontinuity at  $x = 0$ . The resistivity is  $\eta = 0.01$ . Figure 2 shows the numerical solution at  $t = 4.0$  by when the secondary waves created during the development of the dissipative shock structure have left the grid. Again, the shock jump is captured very well but now there are more than 10 grid point in the shock structure. This suggest that shock may be resolved. However, the rather small increase in the shock width between the cases with  $\eta = 0.005$  and  $\eta = 0.01$  shows that numerical dissipation is still important for  $\eta = 0.01$  and only for higher resistivity the shock structure becomes fully resolved (see fig.3).

#### 6.1.3 Alfvén wave

To set up this test we utilized the analytical solution for ideal MHD Alfvén waves obtained in Komissarov(1997). In this test  $\rho = 1.0$ ,  $p = 1.0$ ,  $B^x = 1.0$ , and the Alfvén speed  $c_a = 0.4079$ . Initially the wave occupies the zone  $x_0 < x < x_1$ , with  $x_0 = -0.8$ ,  $x_1 = 0.0$ . To the left of the wave  $\mathbf{B} = (1.0, 0.1, 0.0)$ ,  $\gamma \mathbf{v} = 0$ . In the wave the angle  $\theta$  between the tangential component of magnetic field and the  $y$ -axis varies as

$$\theta = 2\pi(3\xi^2 - 2\xi^3), \quad \xi = (x - x_0)/(x_1 - x_0),$$

that gives vanishing first derivatives at  $x_{0,1}$ . The initial electric field is computed via eq.(68) and the electric charge density via eq.(8). The computational grid is uniform and has 400 cells in  $[-1, +1]$ . The resistivity is set to a relatively small value,  $\eta = 0.003$ , in order to get closer to the ideal case. The simulations are continued up to  $t = 1.5$  and then

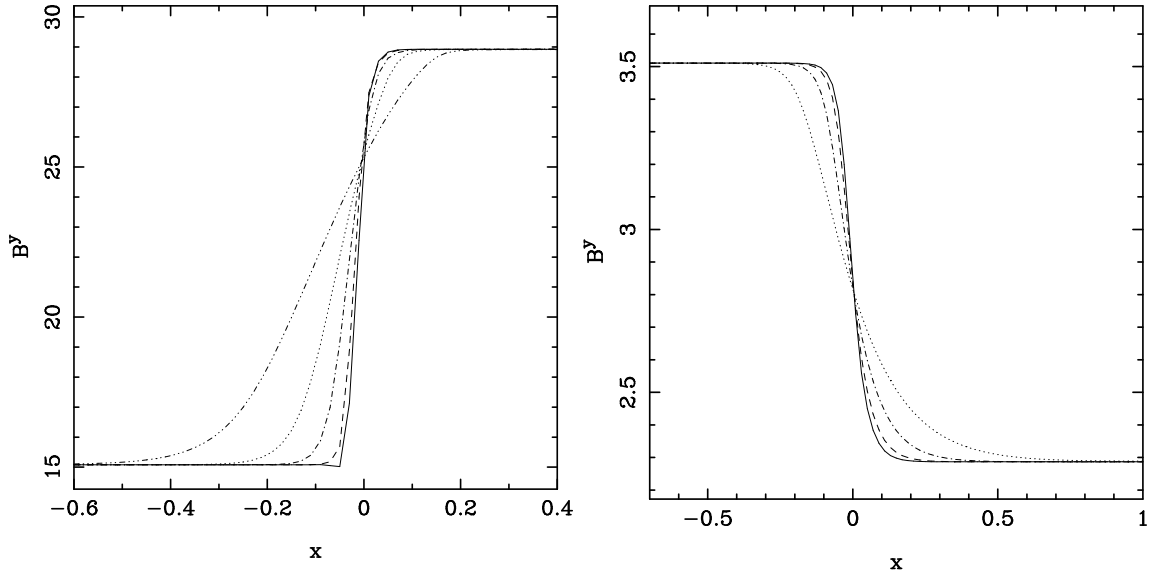


**Figure 3.** Dependence of shock structure on resistivity. *Left panel:* Stationary fast shock for  $\eta = 0.01$  (solid line),  $\eta = 0.03$  (dashed),  $\eta = 0.09$  (dash-dotted),  $\eta = 0.18$  (dotted),  $\eta = 0.36$  (dash-triple-dotted); *Right panel:* Stationary fast shock for  $\eta = 0.01$  (solid line),  $\eta = 0.02$  (dashed),  $\eta = 0.04$  (dash-dotted),  $\eta = 0.08$  (dotted).

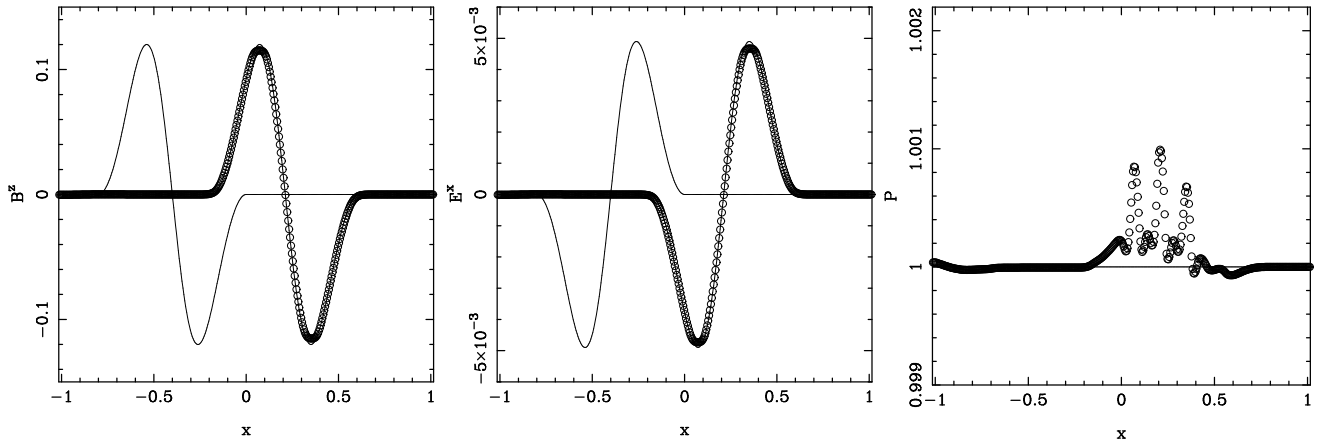


**Figure 4.** Alfvén wave.

compared with the exact solution of ideal MHD at the same time (fig.4). One can see that the agreement is pretty good. The ideal solution keeps the wave profile totally invariant, however the numerical solution is a little distorted, mainly due to numerical dissipation (this is confirmed by studying the dependence on  $\eta$ ).

When the zero gradient boundary conditions (free-flow) are utilised in the simulations then both the fast and the slow waves do not get reflected of boundaries and cleanly pass through. However, the Alfvén waves exhibit noticeable reflection (in contrast to the results with our ideal MHD code). We have not figured out yet as to how to avoid such a reflection.

#### 6.1.4 Self-similar current sheet

Assume that  $\mathbf{B} = (0.0, B(x, t), 0.0)$ , the magnetic pressure is much smaller than the gas pressure everywhere, and  $B(x, 0)$  changes sign within a thin current layer of width  $\Delta l$ . Pro-

vided the initial solution is in equilibrium,  $p = \text{const}$ , the evolution is a slow diffusive expansion of the layer caused by the resistivity and described by the archetypal diffusion equation

$$\partial_t B - \eta \partial_x^2 B = 0.$$

As the width of the layer becomes much larger than  $\Delta l$  the expansion becomes self-similar

$$B(x, t) = B_0 \operatorname{erf} \left( \frac{1}{2\sqrt{\eta\xi}} \right), \quad \xi = t/x^2, \quad (69)$$

where erf is the error function, and this analytic results can be used to test the resistive part of the code. In the test problem that is presented here the initial solution has uniform distribution of  $P = 50.0$ ,  $\rho = 1.0$ ,  $\mathbf{E} = 0$ , and  $\gamma\mathbf{v} = 0$  and the initial magnetic field is given by eq.(69) for  $B_0 = 1.0$ ,  $t = 1$ , and  $\eta = 0.01$ . The computational grid is uniform and has 200 cells in  $[-1.5, +1.5]$ . The numerical simulations are

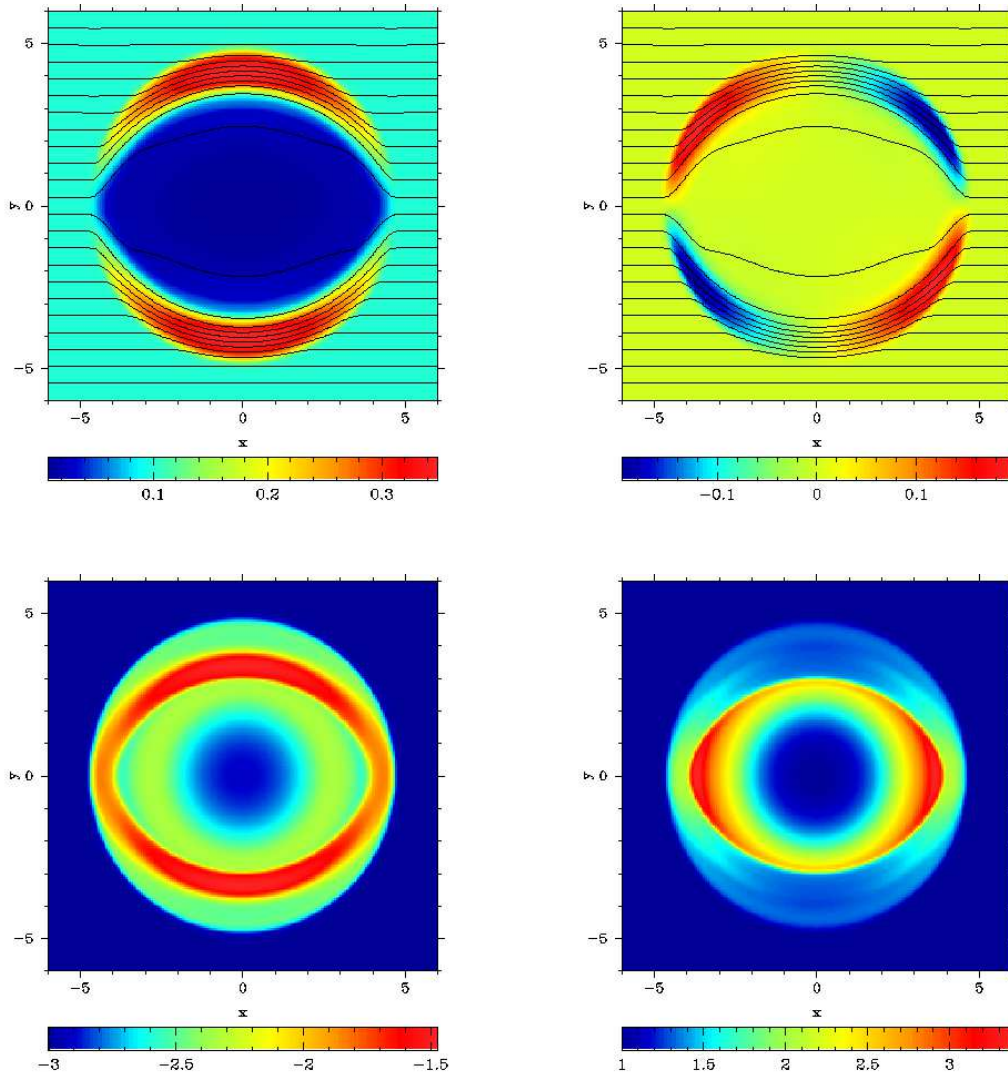


**Figure 6.** Strong cylindrical explosion. *Top left panel:*  $B^x$  and magnetic field lines; *Top right panel:*  $B^y$  and magnetic field lines; *Bottom left panel:*  $\log_{10} p$ , gas pressure; *Bottom right panel:* Lorentz factor.

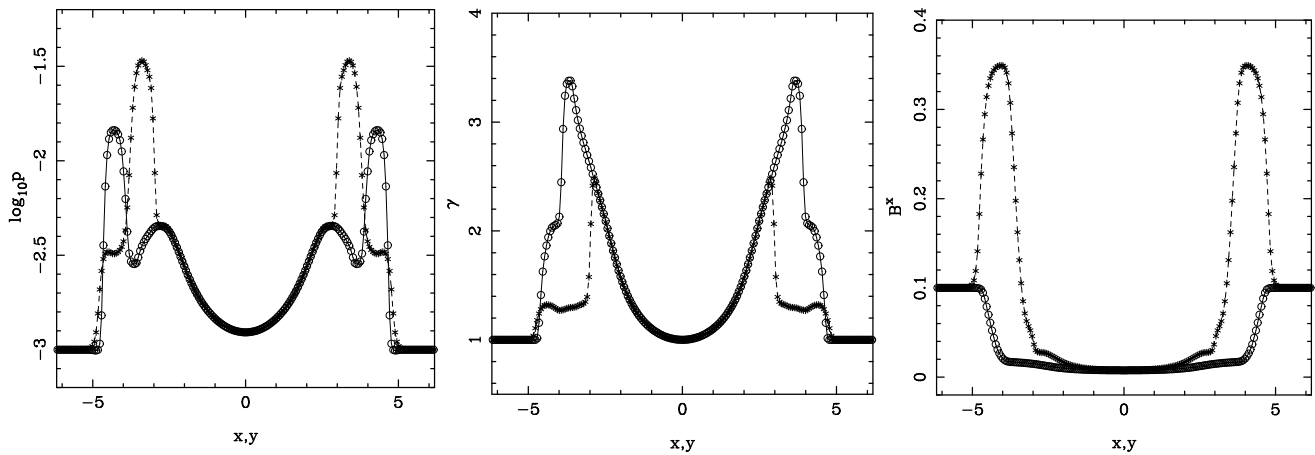


**Figure 7.** Strong cylindrical explosion. This plot show slices along  $x = 0$  (dashed line and stars) and  $y = 0$  (solid lines and circles) for gas pressure (left panel), Lorentz factor (middle panel), and  $B^x$  (right panel).

continued up to  $t = 8$  and then the numerical solution is compared with the solution (69) for  $t = 9$ . The results are shown in figure 5 – one cannot see the difference between the solutions.

## 6.2 Multi-dimensional tests

All the one-dimensional problems, that are described above, have been used to test both the 2D and 3D versions of the code via application in all two/three directions of the Cartesian grid. The results are almost identical to that of 1D tests. In addition we considered several generically multi-dimensional problems.

### 6.2.1 Strong cylindrical explosion

Strong symmetric explosions are useful standard tests for MHD codes even if there are no exact analytic solutions to work with. This is because the generated shocks make all possible angles to the grid and to the magnetic field thus allowing to detect well hidden bugs and to reveal potential weaknesses. In this problem the Cartesian computational domain is  $(-6.0, +6.0) \times (-6.0, +6.0)$  with 200 equidistant grid points in each direction. The initial explosion zone is a cylinder of radius  $r = 1$  centered onto the origin. Its pressure and density are set to  $p = 1$  and  $\rho = 0.01$  for  $r < 0.8$  and exponentially decrease for  $0.8 < r < 1.0$ . The ambient gas has  $p = \rho = 0.001$ . The initial magnetic field is uniform,  $\mathbf{B} = (0.1, 0.0, 0.0)$ . Figure 6 shows the 2D solution at  $t = 4$  for  $\eta = 0.018$  and  $\eta_d = 1/\kappa = 0.18$ . It exhibits the same features as the ideal MHD solution of a similar test problem (Komissarov 1999) which is expected given the low value of  $\eta$  and shows nothing that could be suspected as artifacts. For more detailed future comparisons with other codes figure 7 shows slices of the solution along  $x = 0$  and  $y = 0$ .

The same problem has been used to test the 3D code with identical results.

### 6.2.2 Strong spherical explosion

Finally, we tested our 3D code on the problem of spherical explosion. All parameters of the explosion are the same as in the cylindrical case with exception of the explosion zone - now this is a sphere of unit radius. The computational domain is  $(-6.0, +6.0) \times (-6.0, +6.0) \times (-6.0, +6.0)$  with 140 equidistant grid points in each direction. Figures 8 and 9 show the numerical solution for  $\eta = 0.0257$  and  $\eta_d = 1/\kappa = 0.257$  at  $t = 4.0$ . The general structure of the solution is similar to that of the cylindrical case but with much stronger central rarefaction. One qualitatively new feature is the non-vanishing electric charge density (top right panel of fig.8). Given the axial symmetry of the problem one expects the solutions to be the same in the planes  $z = 0$  and  $y = 0$ . Figure 9 shows that this is indeed the case.

## 7 CONCLUSIONS

We have constructed a multidimensional upwind scheme for resistive relativistic magnetohydrodynamics. At the moment only the case of scalar resistivity has been implemented and

more work has to be done to incorporate the case of tensor resistivity. The results of test simulations show that the scheme is robust in the regime of small to moderate magnetization, which can be described by the ratio of the electromagnetic energy density to the total mass-energy density of matter. The regime of high magnetization is still problematic as the the truncation errors for the energy-momentum of matter become large often making impossible to convert the conserved quantities into the primitive ones. This is a well know problem of all conservative schemes for relativistic MHD. Apart from this drawback the scheme can handle equally well both resistive current sheets and shock waves and thus can be a useful tool for studying phenomena of relativistic astrophysics that involve both colliding supersonic flows and magnetic reconnection.

## ACKNOWLEDGMENTS

This research is funded by PPARC under the rolling grant “Theoretical Astrophysics in Leeds”. The author thanks Matthew Boham for his help in testing the 3D code and Maxim Barkov who is currently working on its parallelization.

## REFERENCES

- Anderson M., Hirschmann E.W., Liebling S.L., Neilsen D., 2006,CQGra,23,6503  
 Anninos P., Fragile P. C., Salmonson J. D., 2005, ApJ, 635, 723  
 Antón L., Zanotti O., Miralles J. A., Martí J. M., Ibáñez J. M., Font J. A., Pons J. A., 2006,ApJ,637,296  
 Blackman E.G., Field G.B., 1993, Phys.Rev.Lett.,71,3481  
 De Villiers J.-P., Hawley J.F., 2003,ApJ,589,458.  
 Del Zanna L., Bucciantini N., Londrillo P., 2003,A&A,400,397  
 Del Zanna L., Zanotti O., Bucciantini N., Londrillo P., 2007, submitted to A&A (arXiv:0704.3206)  
 Duez M.D., Liu Y.T., Shapiro S.L., Stephens B.C., 2005,Phys.Rev.D,72,024028  
 Gammie C.F., McKinney J.C., Toth G., 2003,ApJ,589,444.  
 Godunov S.K., 1959,Mat.Sb.,47,357.  
 Giacomazzo B., Rezzolla L., 2007, Class.Quant.Grav.,24(12),S235  
 Harten A., Lax P.D., van Leer B., 1983, SIAM Rev,25,35.  
 Jackson J.D., 1979, *Classical Electrodynamics*, John Wiley & Sons, New York  
 Koide S., Shibata K., Kudoh T., 1999, ApJ, 522, 727  
 Koldoba A.V., Kuznetsov O.A., Ustyugova G.V., 2002, MNRAS, 333, 932.  
 Komissarov S.S., 1997,Phys.Lett.A,232,435  
 Komissarov S.S., 1999,MNRAS,303,343 Koide S., Shibata K., and Kudoh T., 1999, Ap.J., **522**, 727.  
 Komissarov S.S., 2001, in “Godunov Methods: Theory and Applications”, ed. E.F.Toro, Kluwer, New York, p.519.  
 Komissarov S.S., 2004,MNRAS,350,1431.  
 Lyubarsky Y.E., 2005, MNRAS,358,113.  
 Lyutikov M., Uzdensky D., 2003,ApJ,589,893.  
 McKinney J.C., 2006,MNRAS,367,1797.  
 Mignone A., Bodo G., 2006,MNRAS,368,1040.  
 Mignone A., Bodo G., Massaglia S., Matsakos T., Tesileanu O., Zanni C., Ferrari A., 2007,ApJS,70(1),228.  
 Mizuno Y., Nishikawa K.-I., Koide S., Hardee P., Fishman G.J., 2006, submitted to ApJS (astro-ph/0609004).  
 Munz C.-D.,Omnes P., Schneider R., Sonnendruker E., Vob U., 1999,JCP,161,484.

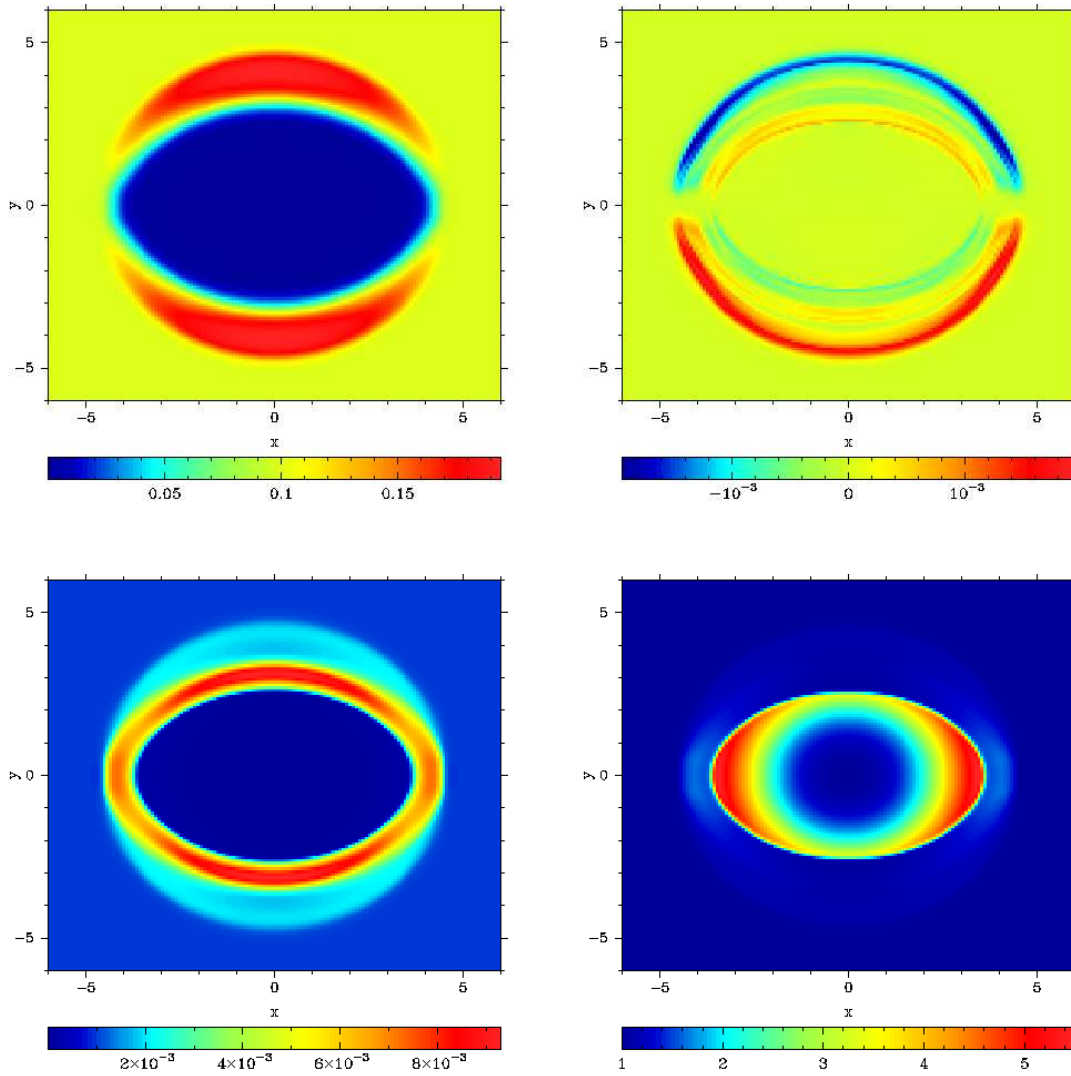


**Figure 8.** Strong spherical explosion. *Top left panel:*  $B^x$ ; *Top right panel:*  $q$ , electric charge density; *Bottom left panel:*  $p$ , gas pressure; *Bottom right panel:* Lorentz factor.

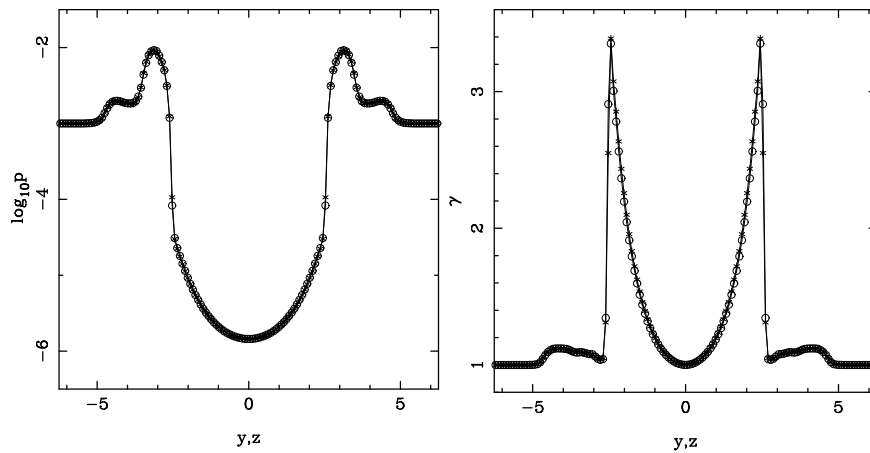


**Figure 9.** Strong spherical explosion. In both panels stars show the solution along the *Left panel:*  $\log_{10} p$ , gas pressure. *Right panel:*  $q$ , electric charge density.

- Neilsen D., Hirschmann E.W., Millward R.S.,  
2006, *Class.Quant.Grav.*, 23(16), S505.
- Noble S.C., Gammie C.F., McKinney, J.C., Del Zanna L.,  
2006, *ApJ*, 641, 626.
- Shibata M., Sekuguchi Y. I., 2005, *Phys.Rev.D.*, 72, 044014
- Strang G., 1968, *SIAM J.Num.Anal.*, 5, 506
- Watanabe N., Yokoyama T., 2006, *ApJ*, 647, L123.